 doi:10.20944/preprints202103.0527.v1

Article

Numerical Analysis of Dynamic Interaction Between Two Closely Spaced Vertical Axis Wind Turbines

Yutaka Hara [1,*], Yoshifumi Jodai [2], Tomoyuki Okinaga [3] and Masaru Furukawa [1]

[1] Faculty of Engineering, Tottori University, 4-101 Koyama-Minami, Tottori, 680-8552, Japan; hara@tottori-u.ac.jp, furukawa@tottori-u.ac.jp
[2] Department of Mechanical Engineering, Kagawa National Institute of Technology (KOSEN), Kagawa College, 355 Chokushi, Takamatsu, 761-8058, Japan; jodai@t.kagawa-nct.ac.jp
[3] Graduate School of Engineering, Tottori University, 4-101 Koyama-Minami, Tottori, 680-8552, Japan; piyomo.smile@gmail.com
* Correspondence: hara@tottori-u.ac.jp; Tel.: +81-857-31-6758

Abstract: To investigate the optimum layouts of small vertical axis wind turbines, a two-dimensional analysis of dynamic fluid body interaction is performed via computational fluid dynamics for a rotor pair in various configurations. The rotational speed of each turbine rotor (diameter: D = 50 mm) varies based on the equation of motion. First, the dependence of rotor performance on the gap distance (*gap*) between two rotors is investigated. For parallel layouts, counter-down (CD) layouts with blades moving downwind in the gap region yield a higher mean power than counter-up (CU) layouts with blades moving upwind in the gap region. CD layouts with gap/D = 0.5–1.0 yield a maximum average power that is 23% higher than that of an isolated single rotor. Assuming isotropic bidirectional wind speed, co-rotating (CO) layouts with the same rotational direction are superior to the combination of CD and CU layouts regardless of the gap distance. For tandem layouts, the inverse-rotating configuration (IR) shows an earlier wake recovery than the CO configuration. For 16-wind-direction layouts, both the IR and CO configurations indicate similar power distribution at gap/D = 2.0. For the first time, this study demonstrates the phase synchronization of two rotors via numerical simulation.

Keywords: wind energy; vertical axis wind turbine; computational fluid dynamics; dynamic interaction; closely spaced arrangements; phase synchronization; wind farm; dryland

1. Introduction

In a wind farm comprising numerous large-scale horizontal-axis wind turbines (HAWTs), the distance between adjacent turbine rotors must be several times longer than the rotor diameter. Otherwise, the power output will decrease significantly when a turbine exists in the wake of the upstream turbine. By predicting the wake of the turbines [1, 2], the optimal layout of turbines that maximizes the wind farm power density (output per unit land area) can be identified—that is an important issue in the wind power field. Although vertical-axis wind turbines (VAWTs) do not prevail currently, as the basis for considering the optimal layout of the VAWT wind farm, Rajagopalan et al. conducted computational fluid dynamics (CFD) simulations assuming a two-dimensional (2D) laminar flow field [3]. Their results indicated that the rotors on the downwind side, but outside of the wake, produced a higher power output than the first-row rotors that faced the undisturbed flow owing to the interactions between the VAWT rotors. Meanwhile, Dabiri et al. proposed the possibility of closely spaced counter-rotating VAWT arrays, which can enhance the wind farm power density to a greater degree than existing HAWT wind farms; they conducted a numerical simulation based on a potential flow model incorporating velocity deficit [4] and field experiments using actual small VAWTs (Windspire: 1.2 kW) [5, 6]. CFD analyses targeting a counter-rotating VAWT pair, which was used by Dabiri as a basis for the rotor array, have been recently conducted by many re-

Preprints (www.preprints.org) | NOT PEER-REVIEWED | Posted: 22 March 2021 doi:10.20944/preprints202103.0527.v1

searchers. Zanforlin and Nishino performed 2D-CFD simulations of rotor models corresponding to Windspire and demonstrated that a counter-rotating closely spaced VAWT pair can produce a larger power output than an isolated single turbine [7]. Chen et al. conducted a 2D-CFD simulation targeting a straight-bladed VAWT pair and investigated the effects of five factors, i.e., inflow angle, tip speed ratio, turbine spacing, rotational direction, and blade angle, on the performance of a dual-turbine system [8]. Their results indicated that the power output of the rotor pair depended primarily on the tip speed ratio and inflow angle. De Tavernier et al. [9] comprehensively investigated the effects of rotor load (solidity), rotor spacing, and inflow angle on the flow and power output of a closely spaced 2D rotor pair (rotor radius = 10 m) via a 2D-CFD simulation based on a panel/vortex model. Ma et al. performed a 2D-CFD analysis to simulate a vertical axis twin-rotor tidal current turbine, in which the two rotors revolved in opposite directions [10]. Based on the analysis, the maximum power coefficient was obtained at a tip speed ratio of 1.5, where the ratio of the rotor spacing to the diameter in the layout of the main flow perpendicular to the centerline connecting the two rotor centers was 9/4. As the rotor spacing became smaller than the optimal value, the power output decreased. In all four CFD analyses, the rotational speeds of two rotors were fixed to the same value in each run of the calculation. In terms of basic studies pertaining to a rotor pair normal to the main flow, Bearman and Wadcock [11] experimentally investigated the interaction between a circular cylinder pair, whereas Yoon et al. [12] performed a CFD analysis on a rotating circular cylinder pair. The flow patterns around a circular cylinder pair might be analogous to the flow patterns around a turbine rotor pair in terms of spacing dependence. However, it is important to recognize the essential difference in the manner by which vortices are shed between a solid circular cylinder and a turbine rotor comprising blades. Recently, Vergaerde et al. [13] performed experiments using a closely spaced pair of straight-bladed VAWTs that mutually revolved in opposite directions in a wind tunnel and observed their phase synchronization. The first author of this paper and his colleagues have proposed a concept named "Wind Oasis" [14], which applies a wind farm comprising small-scale vertical-axis-type butterfly wind turbines (BWTs) [15] for agriculture in drylands to pump water for crops and to generate electricity for people. As basic studies for materializing this concept, the authors of the present paper have been conducting wind tunnel experiments using miniature BWT models and performing the 2D-CFD analysis of the corresponding rotors. Although not described in detail herein, Jodai et al. [16, 17] observed phase synchronization in their experiments on a closely spaced miniature BWT pair as well.

In this study, to determine the optimal layout of a VAWT wind farm, a CFD analysis of a 2D vertical-axis rotor pair was performed considering the dynamic interaction between a fluid and wind turbines (i.e., the dynamic fluid-body interaction, DFBI [18]). In contrast to the aforementioned conventional CFD simulations, in this study, the rotational speed of each rotor was not fixed to a constant value but was simulated based on the equation of motion of the rotor. This CFD analysis using the DFBI is equivalent to experiments involving variable-speed wind turbines. Although some of the results have been reported in several oral presentations [19-22] and in a commentary article [14], they are integrated herein and new considerations and results are included; furthermore, the calculation times of some cases were prolonged until the rotor angular velocities converged within the new criteria. The details of the revised data acquisition are explained in the following section. The important results of this study are as follows: In the parallel layouts perpendicular to the main flow, the counter-down layouts (CD: the blades moving downwind in the gap part) yielded a higher mean power than the counter-up layouts (CU: the blades moving upwind in the gap part). In particular, the mean power in the CD layouts with gap/D = 0.5–1.0 was 23% higher than that of an isolated single rotor. By assuming an isotropic bidirectional wind speed, the co-rotating layouts (CO: two rotors in the parallel layout with the same rotational direction) was superior to the combination of CD and CU layouts at any gap distance. For the tandem layouts along the main flow, the inverse-rotating (IR) configuration showed an earlier recovery in terms of the mean rotor

Preprints (www.preprints.org) | NOT PEER-REVIEWED | Posted: 22 March 2021 doi:10.20944/preprints202103.0527.v1

power compared with the CO configuration as the gap distance increased. Based on an analysis of 16-wind-direction configurations, it was discovered that the distributions of the mean power in the IR and CO configurations were similar when the gap distance was twice the rotor diameter. Meanwhile, it was demonstrated that the mean power of the CO configuration was higher than that of the IR configuration for a short gap, under the assumption of an isotropic 16-directional wind speed. To our best knowledge, our current study is the first study where a CFD analysis of the phase synchronization of a rotor pair is conducted, and it is revealed that a phase shift of $\pi/2$ occurred between the angular velocity and torque differences of two rotors.

2. Methods

In this study, a CFD analysis was performed using a 2D rotor, as shown in Figure 1 (b) (hereinafter 2D-CFD rotor) as a target, which corresponds to the equator-level cross section of a three-dimensionally printed model, as shown in Figure 1(a) (hereinafter 3D-EXP rotor). The 3D-EXP rotor (diameter: D = 50 mm, height: H = 43.4 mm, chord length: c = 20 mm, blade cross section: NACA 0018) was used in the wind tunnel experiments performed in another study in parallel [16]. The 2D-CFD rotor did not include the hub and slant blade parts of the 3D-EXP rotor. The solidity of the 2D-CFD rotor used in this study was $\sigma = Bc/(\pi D) = 0.38$ (B: number of blades), which is larger than the solidity ($\sigma = 0.10$) of the rotor of Zanforlin and Nishino [7], that ($\sigma = 0.15$) of the rotor of Chen et al. [8], that ($\sigma = 0.032$) of the rotor of De Tavernier et al. [9], and that ($\sigma = 0.176$) of the rotor of Ma et al. [10]. The trailing edges of the blades of the 2D-CFD rotor were designed to be rounded with the curvature radius of 0.32 mm, in accordance with the 3D-EXP rotor.

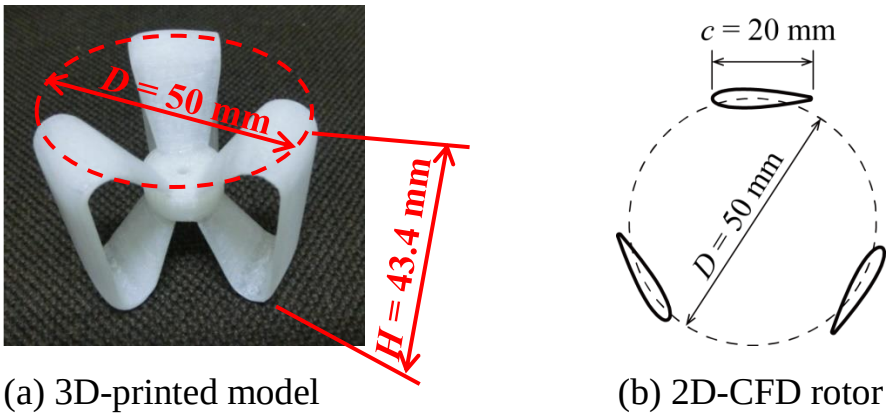

Figure 1. Target rotors of this study: (a) Three-dimensionally printed model (3D-EXP rotor); (b) 2D-CFD rotor used for CFD analysis.

In this study, the commercial application software STAR-CCM+ ver.14.04.011 was used as the numerical solver. The 2D unsteady incompressible Reynolds-averaged Navier-Stokes equations and the equation of continuity were solved by adopting the k–ω shear stress transport (SST) turbulence model [23]. A trim mesh was selected for the entire domain except for the region near the blade surfaces, where a prism layer mesh was used to create 15 layers that thinned progressively. The rotating motion of the rotor was realized using the overset mesh method. First, the torque performance (Q vs ω; Q is the torque, and ω is the angular velocity) of an isolated single rotor was simulated at four wind speeds (U_∞ = 6, 8, 10, and 12 m/s). The entire calculation domain of the CFD analysis of the single rotor was a rectangle measuring $40D \times 50D$; the rotor center was positioned at $20D$ from the inlet boundary. Each run of the calculations were performed under a fixed rotational speed and was continued until the 10th rotor rotation was completed. The torque in the last five rotations of each run was averaged, and the results are shown in Figure 2.

Preprints (www.preprints.org) | NOT PEER-REVIEWED | Posted: 22 March 2021 doi:10.20944/preprints202103.0527.v1

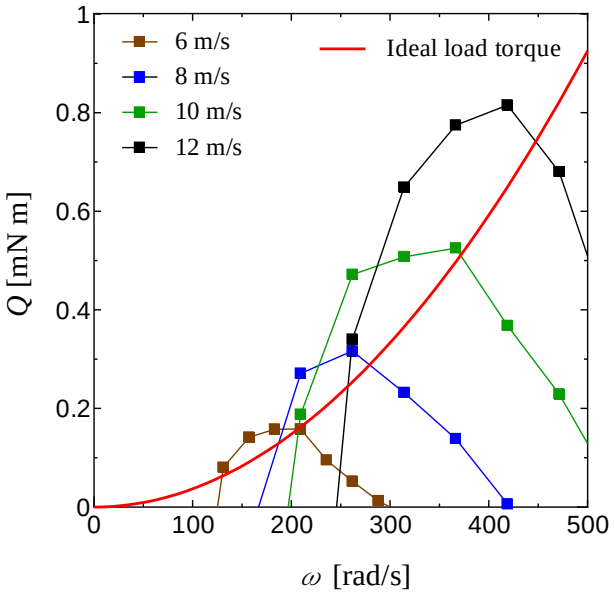

Figure 2. Torque curves of 2D-CFD rotor and ideal load torque curve. Values of torque were converted to corresponding values of 3D-EXP rotor.

The 2D calculation in STAR-CCM+ provided results that corresponded to the model with unit thickness, i.e., 1 m. Therefore, all the raw output values of the CFD analysis were multiplied by 0.0434, as shown in Figure 2, to convert them into torque values corresponding to those of the 3D-EXP rotor. The curve in red in Figure 2 represents the ideal load torque that passes a point that is 95% of the maximum power obtained via CFD analysis for a wind speed of 10 m/s. The load torque Q_L [N m] is expressed as follows:

$$Q_L = 3.71 \times 10^{-9} \omega^2. \quad (1)$$

In the CFD analysis based on the DFBI method, the time-dependent angular velocity of each rotor is determined by solving the following equation of motion:

$$I \frac{d\omega}{dt} = Q_R - Q_L. \quad (2)$$

In Equation (2), I is the moment of inertia of each rotor. When the mass of 3D-EXP rotor was assumed to be 14 g, the moment of inertia was estimated to be 5.574×10^{-6} kg m^2 based on a computer-aided design (CAD) model. For the actual CFD analysis, the value of $I = 5.574 \times 10^{-6}$ kg m^2 × 1000 mm / 43.4 mm = 1.284×10^{-4} kg m^2 was set in STAR-CCM+ because the 2D-CFD rotor had a unit length height. The Q_R term on the right-hand side of Equation (2) represents the rotational torque of each rotor obtained from CFD calculation. As for the load torque Q_L, the value of 1000/43.4 × Equation (1) (i.e., 8.55×10^{-8} ω^2) was set in STAR-CCM+.

The parallel layouts of the two rotors, in which the line connecting the two rotor centers (y-axis direction) is perpendicular to the main flow (x-axis direction), include the three layouts shown in Figures 3(a)-(c). In the CO layout (Figure 3(a)), the upper rotor (Rotor 1: R1) and lower rotor (Rotor 2: R2) rotate in the same direction; in the CD layout (Figure 3(b)), R1 and R2 rotate in different directions, and the blades move in the same direction as the main flow between the two rotor centers; in the CU layout (Figure 3(c)), the two rotors revolved in different directions and the blades moved against the main flow between the rotor centers. The terminology for the parallel layouts is based on De Tavernier et al. [9]. In this study, the CFD analysis was performed using the DFBI method (hereinafter DFBI-CFD) on a rotor pair comprising two 2D-CFD rotors in the aforementioned three parallel layouts, i.e., CO, CD, and CU, with different rotor spacings (gaps) of 10, 15, 25, 50,100, and 200 mm.

Preprints (www.preprints.org) | NOT PEER-REVIEWED | Posted: 22 March 2021 doi:10.20944/preprints202103.0527.v1

The tandem layouts of the two rotors, in which the line connecting the two rotor centers is parallel to the main flow direction, are classified into the two layouts shown in Figures 3 (d) and (e). In this study, the layouts shown in Figures 3(d) and 3(e) are classified as the tandem co-rotating (TCO) and tandem inverse-rotating (TIR) layouts, respectively. The DFBI-CFD analysis was performed for the TCO and TIR layouts with the gaps of 25, 50,100, 200, 300, 400, and 500 mm.

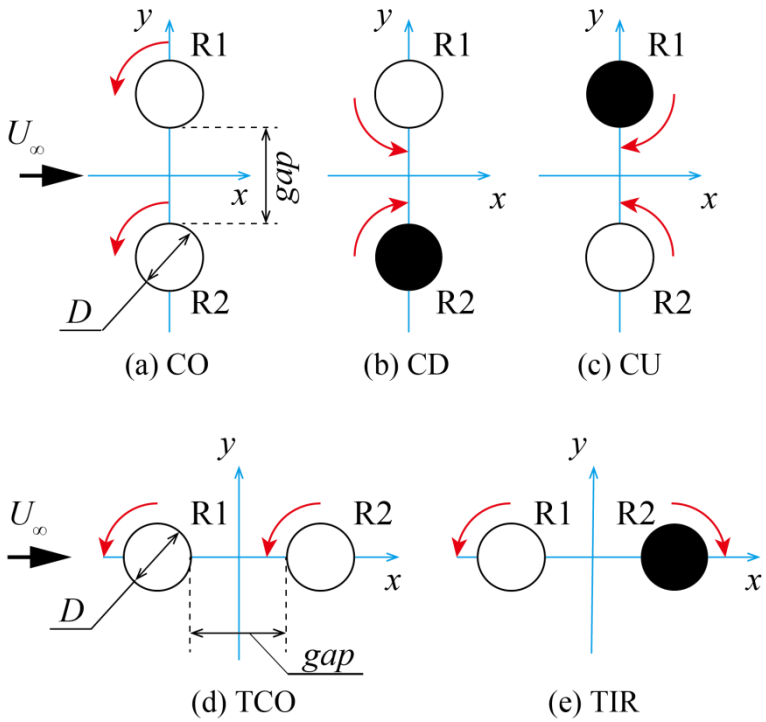

Figure 3. Specific layouts of a pair of VAWT rotors: (a) co-rotating (CO) layout; (b) counter-down (CD) layout; (c) counter-up (CU) layout; (d) tandem co-rotating (TCO) layout; (e) tandem inverse-rotating (TIR) layout.

After executing the DFBI-CFD calculations for the parallel and tandem layouts, the 16-wind-direction configurations shown in Figure 4 were analyzed using similar methods. The cases shown in Figure 4(a), in which two rotors rotate in the same direction, are defined as the CO configurations, whereas the cases shown in Figure 4(b), in which two rotors rotate mutually in different directions, are termed as inverse-rotation (IR) configurations in the present study. The coordinate system (x_R, y_R) depicted in Figure 4 is fixed at the rotor pair, and the origin is placed at the center of the rotor pair. The origin of the wind-direction angle θ is defined in the left-hand side of the rotor pair, i.e., as the direction of $-x_R$, in this analysis. For the five specific layouts shown in Figure 3, the CO layout corresponds to the case of $\theta = 0$ ° in the CO configurations; the case of $\theta = 180$ ° is identical to the CO layout and is not clearly indicated in Figure 4(a); the TCO layout corresponds to the case of $\theta = 90$ ° in the CO configurations; the case of $\theta = 270$ ° is equivalent to the TCO layout, but the terms are not indicated in the same manner as that of the CO layout. The terms CD, CU, and TIR are shown in the corresponding parts in Figure 4(b). It is clear from Figure 4 that the same layout exists in the symmetrical direction with respect to the center of the rotor pair (i.e., origin symmetry) in the CO configurations. By contrast, an equivalent case was observed in the symmetrical direction with respect to the x_R-coordinate axis (i.e., line symmetry) in the IR configurations. Therefore, the DFBI-CFD analysis was performed for approximately half of the cases of the 16-wind-direction configurations, and the results of the equivalent layout were substituted for those of the counterpart. The DFBI-CFD analysis for the 16-wind-direction configurations was conducted under the gaps of 25, 50, and 100 mm.

Preprints (www.preprints.org) | NOT PEER-REVIEWED | Posted: 22 March 2021 doi:10.20944/preprints202103.0527.v1

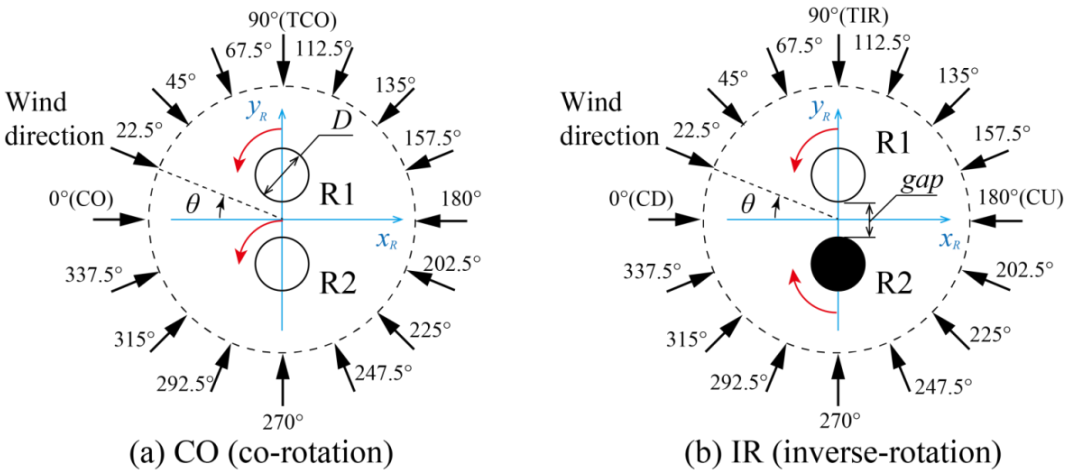

Figure 4. Definition of 16-wind-direction configurations: (a) co-rotation (CO) configurations; (b) inverse-rotation (IR) configurations.

Figure 5 shows the mesh for the DFBI-CFD analysis of the rotor pair. The entire calculation domain was a rectangular region measuring 80D×100D, and the center of the rotor pair was located at 40D from the inlet boundary. The mesh adopted for most parts of the entire domain was a trim mesh, and 15 layers of the prism layer mesh were created near the blade surfaces. The maximum value of y+, which is the non-dimensional distance of the first cell from the blade surface, was approximately 0.35 in any case. The overset mesh enabled the rotation of two rotors, even in the closest spacing of gap/D = 0.2. The number of cells in the static region was approximately 180000, and that in two rotating regions added together was approximately 100000; the total number of cells was approximately 280000. The upstream uniform wind speed was fixed at U_∞ = 10 m/s for all simulations of the rotor pair. Owing to the interaction between the fluid and rotors, the rotational speed of each rotor varied based on the local flow condition as time progressed. When it was difficult to predict the converged value in advance, the initial angular velocity of each rotor was set to 366 rad/s, which was similar to the converged angular velocity ω_{SI} obtained in the DFBI-CFD analysis of an isolated single 2D-CFD rotor; when the converged angular velocity can be predicted, the value was set as the initial value. The initial phases of the two rotors in the CO layout shown in Figure 5(b) had a phase difference of $\pi/3$. However, for the other layouts, a unified initial phase condition was not set. Each calculation was performed until the results converged sufficiently; all the cases reported herein were calculated for 4 s at the least. The criterion of convergence was unified, i.e., when the root mean square (RMS) of the angular velocity in the final 1 s is less than 5 rad/s and the gradient of the linear approximation of the angular velocity in the final 1 s becomes less than 10 rad/s^2, then the DFBI-CFD simulation is stopped and the data such as the torque are averaged during the final 1s. The time step was 2.5×10^{-5} s. The Reynolds number based on the rotor diameter was Re = 3.3×10^4, and that based on the blade chord length was approximately Re_b = 1.2×10^4.

Preprints (www.preprints.org) | NOT PEER-REVIEWED | Posted: 22 March 2021 doi:10.20944/preprints202103.0527.v1

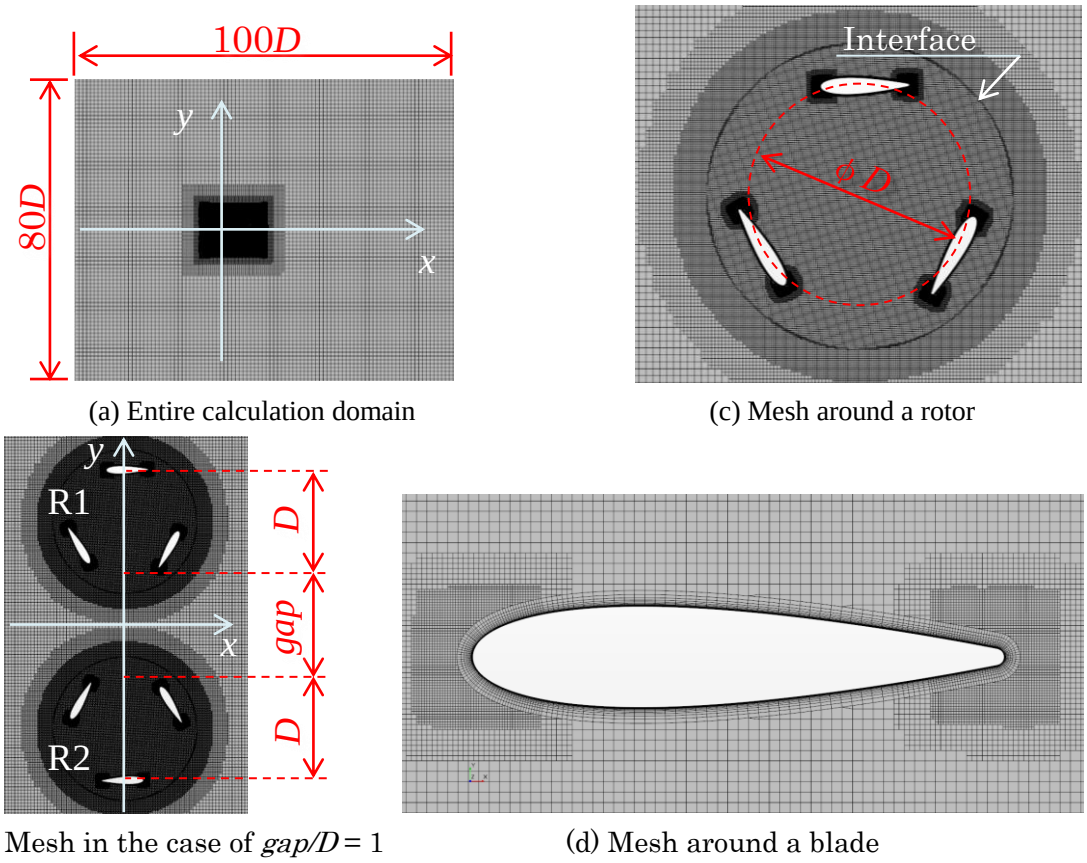

(a) Entire calculation domain

(c) Mesh around a rotor

(b) Mesh in the case of $gap/D = 1$

(d) Mesh around a blade

Figure 5. Calculation domain and mesh used in this study.

The DFBI-CFD analysis of an isolated single rotor under U_∞ = 10 m/s yielded the following results as values equivalent to those of the 3D-EXP rotor: angular velocity, ω_{SI} = 366.1 rad/s (revolution per minute, N_{SI} = 3496 rpm); rotor torque, Q_{SI} = 0.485 mN m; output power, P_{SI} = 177.6 mW. In the following sections, the results of the rotor pair obtained from the DFBI-CFD analysis are expressed using the values divided by the single-rotor values, i.e., the normalized angular velocity ω_{norm}, normalized torque Q_{norm}, and normalized power P_{norm}.

3. Results and Discussion

In this section, results of the DFBI-CFD analysis on the rotor pair are presented and discussed. The following four subsections are presented: Subsection 3.1., gap dependence of parallel layouts; Subsection 3.2., gap dependence of tandem layouts; Subsection 3.3., gap and wind direction dependence of the 16-wind-direction layouts; and Subsection 3.4., phase synchronization of the rotor pair.

3.1. Gap Dependence of Parallel Layouts

As examples of the CFD calculation for the parallel layouts, Figures 6(a)-(c) show the distributions of the x-direction component of flow velocity around a rotor pair with gap/D = 0.5, for CO, CD, and CU layouts. As shown in the CO layout in Figure 6(a), the wake of each rotor deflected upward significantly. As shown in the CD layout in Figure 6(b), the fluid accelerated considerably between the two rotors; the acceleration in the CU layout shown in Figure 6(c) was less than that in the CD layout.

Preprints (www.preprints.org) | NOT PEER-REVIEWED | Posted: 22 March 2021 doi:10.20944/preprints202103.0527.v1

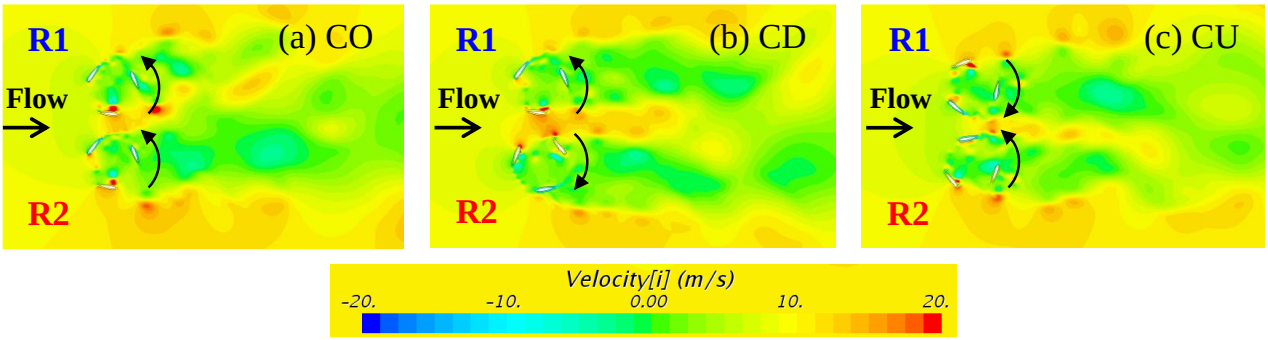

Figure 6. Color contours of flow velocity (*x*–direction component) when *gap*/*D* = 0.5: (a) CO layout; (b) CD layout; (c) CU layout.

The time variation in the angular velocity of each rotor in the parallel layouts (*gap*/*D* = 0.5) shown in Figure 6 is depicted in Figure 7 from the start of the calculation to 4 s. Figure 7 shows the results of the moving average based on a time width of 0.01 s. The initial value of all the cases shown in Figure 7 was 366 rad/s, which was similar to the converged angular velocity ω_{SI} of an isolated single rotor. As shown in Figure 6(a), the two rotors in the CO layout rotated counterclockwise to the main flow emanating from the left-hand side, and the angular velocity of R2 increased owing to the induced velocity of R1, as shown in Figure 7(a). Meanwhile, the angular velocity of R1, which was affected by the induced velocity of R2, did not decrease but increased slightly. As shown by the CD layout shown in Figure 7(b), the angular velocities of the two rotors increased as much as that of R2 in the CO layout because the inflow to both rotors was enhanced by the mutual induced velocities. Because the direction of the induction in velocity in the CU layout shown in Figure 7(c) was opposite to that in the CD layout, the inflow to the rotors reduced. Therefore, the angular velocities of the two rotors were at the same level as the initial value or decreased slightly.

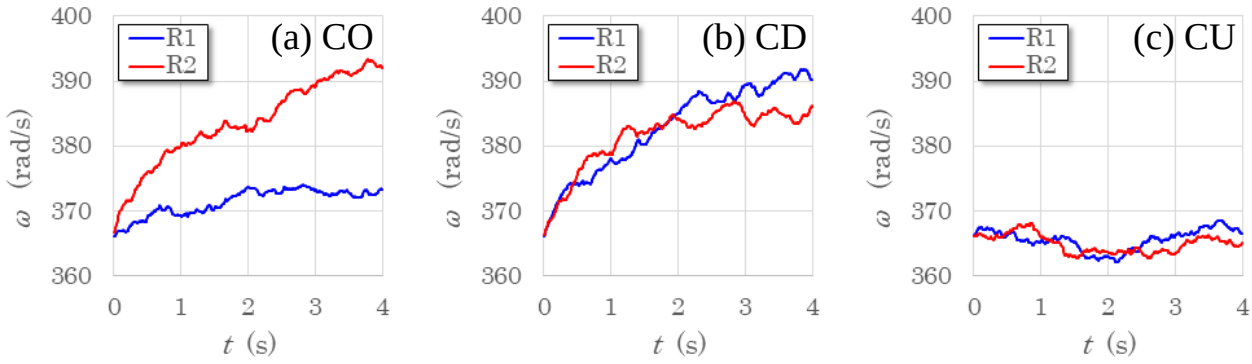

Figure 7. Time variation of angular velocity of each rotor when *gap*/*D* = 0.5: (a) CO layout; (b) CD layout; (c) CU layout.

Figure 8 shows the gap dependence of the normalized angular velocity of each rotor in the CO, CD, and CU layouts. The white squares represent the average values of rotors R1 and R2. The angular velocity ω_2 of R2 was always larger than the angular velocity ω_1 of R1 in the CO layout, and the values of these two angular velocities were similar in the CD and CU layouts at any gap length. Regardless of the layout type, as the gap decreased, the normalized angular velocity increased gradually until *gap*/*D* reached at 0.5–1.0 and decreased rapidly after crossing the peak. This can be attributed to the blockage effects caused by gap narrowing, which is similar to the case of two closely spaced side-by-side circular cylinders. As the gap length approached zero, the rotor pair resembled a bluff body, and most of the inflow could not pass through the rotor gap region. Previous studies pertaining to two side-by-side circular cylinders indicated that the vortex shedding from a closely spaced cylinder pair was similar to that from a sin-

Preprints (www.preprints.org) | NOT PEER-REVIEWED | Posted: 22 March 2021 doi:10.20944/preprints202103.0527.v1

gle-bluff-body, and that the mean drag coefficient of the cylinder pair increased as the gap narrowed [24]. Comparing the averaged values of the normalized angular velocities shown in Figures 8(a)-(c), the relation CD > CO > CU was evident.

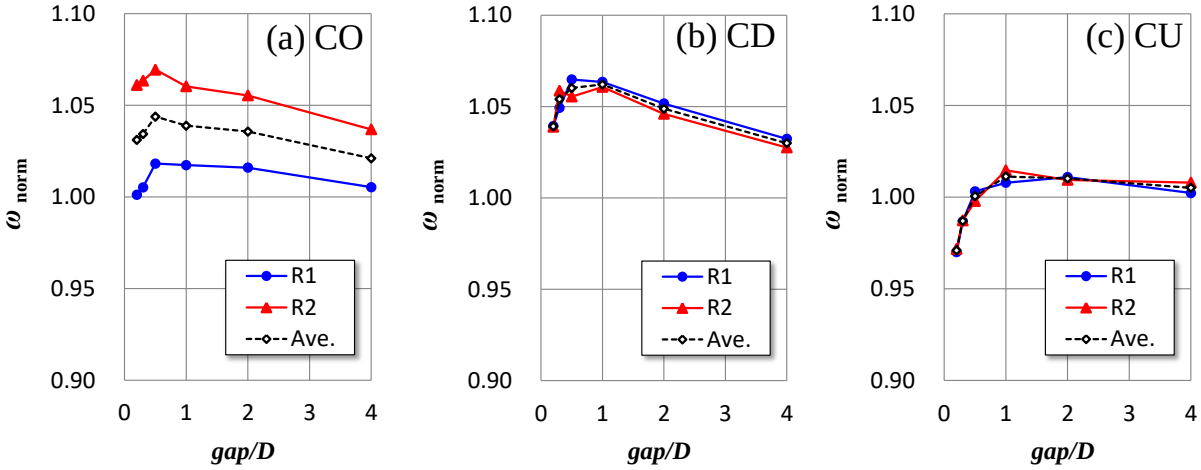

Figure 8. Gap dependence of normalized angular velocity of each rotor: (a) CO layout; (b) CD layout; (c) CU layout.

The gap dependence of the normalized torque shown in Figure 9 is more complicated than that of the angular velocity. In the CO layout, as the gap length decreased, the difference in torque between the two rotors increased; the torque Q_2 of R2 was larger than the torque Q_1 of R1 at any gap length. Meanwhile, the magnitude correlation between Q_1 and Q_2 depended on *gap*/*D* in the CD and CU layouts. This was likely due to the dependence of the mean torque on the averaging period and timing, as the fluctuation in the torque was significant. The torque of R1 tended to decrease, and the torque of R2 abruptly increased as the gap became extremely small in the CO layout (Figure 9(a)). In the CD layout (Figure 9(b)), the averaged torque between Q_1 and Q_2 increased as the gap decreased until *gap*/*D* became 1.0, and as the gap space decreased after crossing the peak, the averaged torque decreased, whereas the torque of each rotor varied significantly. The average torque in the CU layout (Figure 9(c)) increased gradually until *gap*/*D* became 1.0 as the gap decreased, whereas it decreased abruptly when *gap*/*D* was less than 1. The rotation torque of a vertical-axis-type rotor depends significantly on the inflow angle and angle of attack, which are functions of the azimuth angle. The direction of flow (secondary flow) around the rotor significantly affects the torque behavior when the gap space is small.

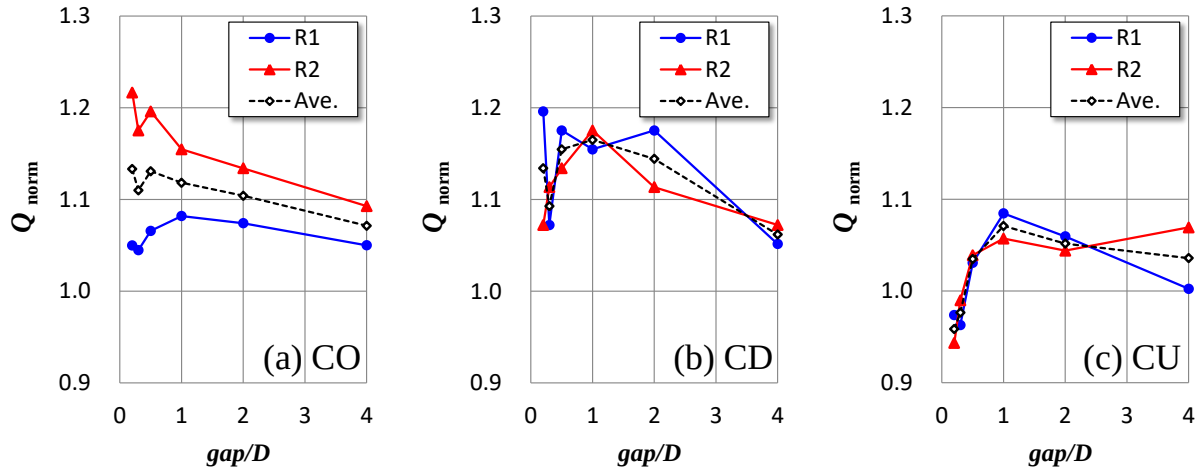

Figure 9. Gap dependence of normalized torque of each rotor: (a) CO layout; (b) CD layout; (c) CU layout.

Preprints (www.preprints.org) | NOT PEER-REVIEWED | Posted: 22 March 2021 doi:10.20944/preprints202103.0527.v1

The normalized power shown in Figure 10, which was obtained by multiplying the angular velocity and torque, indicates a gap dependence similar to that of the normalized torque shown in Figure 9. Considering the mean values of R1 and R2, the normalized power of the parallel layouts increased in the order of CD > CO > CU. This differs from the numerical results obtained by De Tavernier et al. [9] (σ = 0.032). It is unclear whether this was caused by the DFBI method. The results of the present DFBI-CFD analysis differed from the experimental results of Vergaerde et al. [13], where the relation CU > CD was obtained for a pair of two-bladed VAWT rotors with small solidity (the exact value is unknown). Although the experimental results using the 3D-EXP rotors (σ = 0.38) are not explained herein, the wind tunnel experiments showed the common relation CD > CU for the present numerical simulation. Furthermore, Zanforlin and Nishino [7] obtained the same relation (CD > CU) via CFD analysis using 2D rotors with σ = 0.102. The results above suggest that the rotor solidity might be related to the magnitude correlation pertaining to the power of the CD and CU layouts. An important finding is that the mutually counter-rotating rotor pair (the CD layout in this study) can yield a 23% higher average power than an isolated single rotor by approaching the two rotors to a distance of *gap*/*D* = 0.5–1, as shown in Figure 10(b). This implies that, if the prevailing wind of a site has a high probability of appearance in a specific direction, appropriately installing a pair of VAWTs may generate more electricity than that expected from a single turbine. Moreover, as suggested by Dabiri [5], a wind farm comprising many VAWT pairs with the same appropriate configuration against the prevailing wind direction might achieve a high power density. However, further studies must be conducted for confirmation.

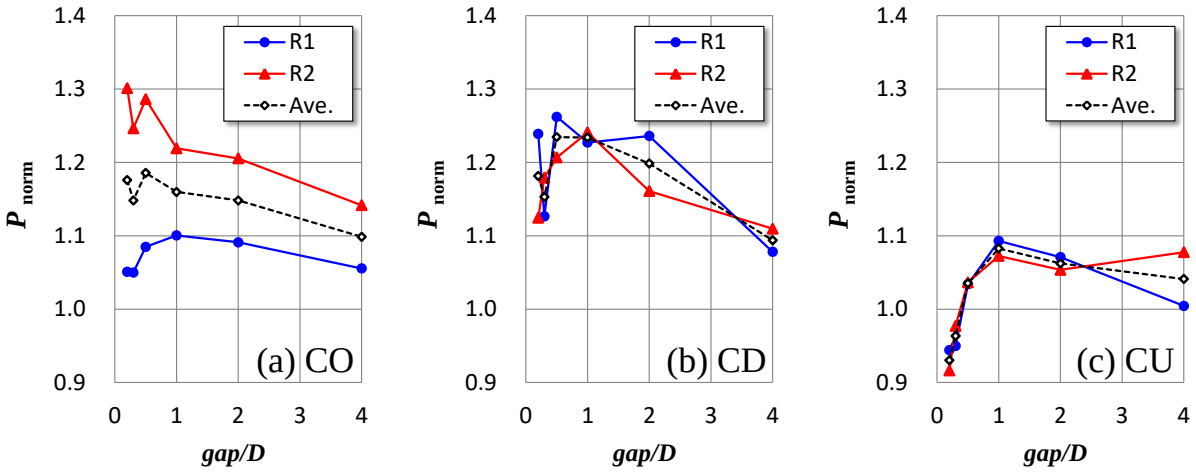

Figure 10. Gap dependence of normalized power of each rotor: (a) CO layout; (b) CD layout; (c) CU layout.

A comparison between the normalized power in the CO layout and the averaged value of the normalized powers of the CD and CU layouts is tabulated in Table 1 for each gap length. This corresponds to the comparison between the CO configuration and IR configuration, where a rotor pair is installed in a parallel layout under the assumption of an isotropic bidirectional wind speed. As shown in Table 1, the CO configuration yielded a higher output power than the IR configuration at any gap space in the ideal bidirectional wind condition.

Table 1. Averaged values of normalized powers under assumption of isotropic bidirectional wind speed.

Layout	*gap*/*D* = 0.2	*gap*/*D* = 0.3	*gap*/*D* = 0.5	*gap*/*D* = 1	*gap*/*D* = 2	*gap*/*D* = 4
CO	1.176	1.148	1.186	1.160	1.148	1.099
Ave. CD & CU	1.056	1.058	1.135	1.158	1.130	1.068

Preprints (www.preprints.org) | NOT PEER-REVIEWED | Posted: 22 March 2021 doi:10.20944/preprints202103.0527.v1

3.2. Gap Dependence of Tandem Layouts

Examples of the DFBI-CFD results presented as color contours of flow velocity (x-direction component) around the tandem layouts are illustrated in Figure 11. Figures 11(a) and (b) show results of the TCO layouts; (c) and (d), the TIR layouts; (a) and (c), case of gap/D = 1; and (b) and (d), case of gap/D = 10. In the case involving a short gap length (Figures 11(a) and (c)), the downwind rotor R2 was almost completely within the wake of the upwind rotor R1. As the two rotors rotated in the same direction in the TCO layout shown in Figure 11(a), the flow speed in the region below the rotor pair became higher than that in the region above because of the constructive interference caused by the induced velocities. In the case involving a long gap length (Figures 11(b) and (d)), although the effects of the wake of R1 on R2 became less prominent, part of the meandering wake of R1 flowed into R2.

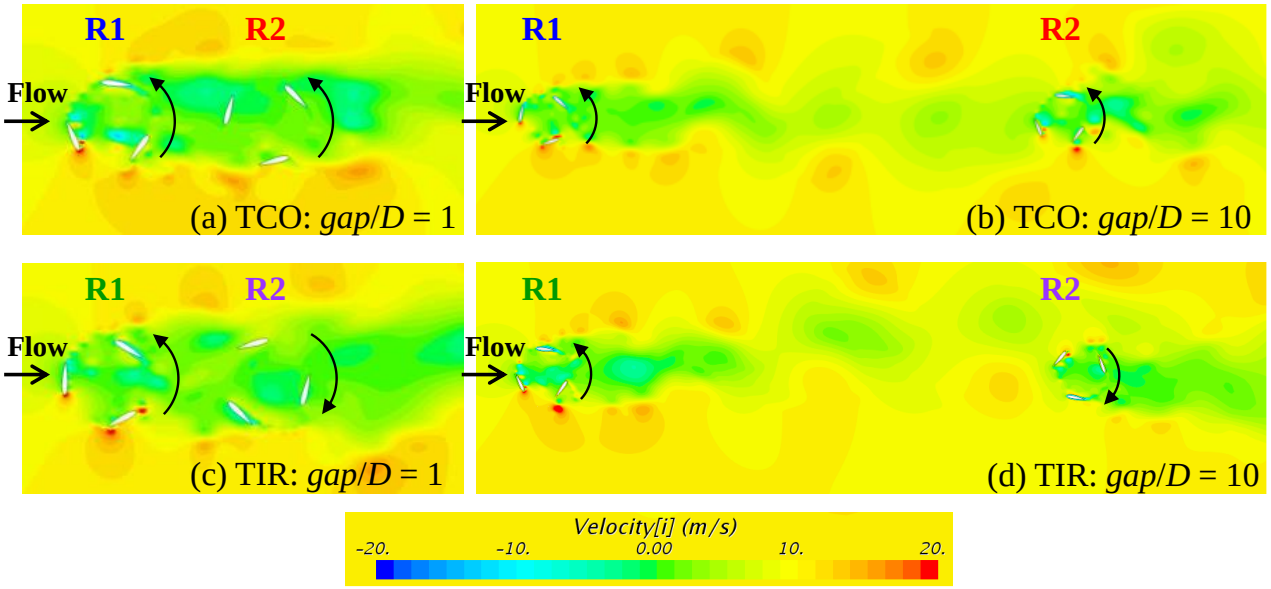

Figure 11. Color contours of flow velocity (x-direction component): (a) TCO layout, gap/D = 1; (b) TCO layout, gap/D = 10; (c) TIR layout, gap/D = 1; (d) TIR layout, gap/D = 10.

Figures 12(a) and (b) show the gap dependence of the normalized angular velocity and normalized power of each rotor in the tandem layouts, respectively. As shown in Figure 12(a), the angular velocity of the upwind rotor R1 was smaller than that of an isolated single rotor until the gap space reached gap/D = 8, indicating the effect of downwind rotor R2 on upwind rotor R1. Even in the case where the two rotors separated from each other and reached a length of gap/D = 10, the angular velocity of R2 was 70%–80% that of an isolated single rotor, and the power was 40%–50%. The three-dimensional CFD analysis of a straight-bladed VAWT conducted by Miyashita et al. [25] demonstrated approximately 90% wake recovery at a distance of x/D ~ 0.5. Therefore, the slow recovery of the wake shown in Figure 12 is attributable to the 2D calculation. The gap dependence of the angular velocity and the power between the TCO and TIR layouts differed only slightly until gap/D = 6. Beyond gap/D = 8, however, the power of the downwind rotor R2 in the TIR layout became larger than that in the TCO layout. Comparing Figures 11(b) and (d), it was observed that in the TCO layout, the induced velocity of the downwind rotor R2 (rotating counterclockwise) caused the upward-deflected wake of the upwind rotor R1 (rotating counterclockwise) in front of R2 to be drawn downward; meanwhile, in the TIR layout, as the induced velocity of R2 (rotating clockwise) deflected the wake of R1 further, the region with higher velocity flowed into R2.

Preprints (www.preprints.org) | NOT PEER-REVIEWED | Posted: 22 March 2021 doi:10.20944/preprints202103.0527.v1

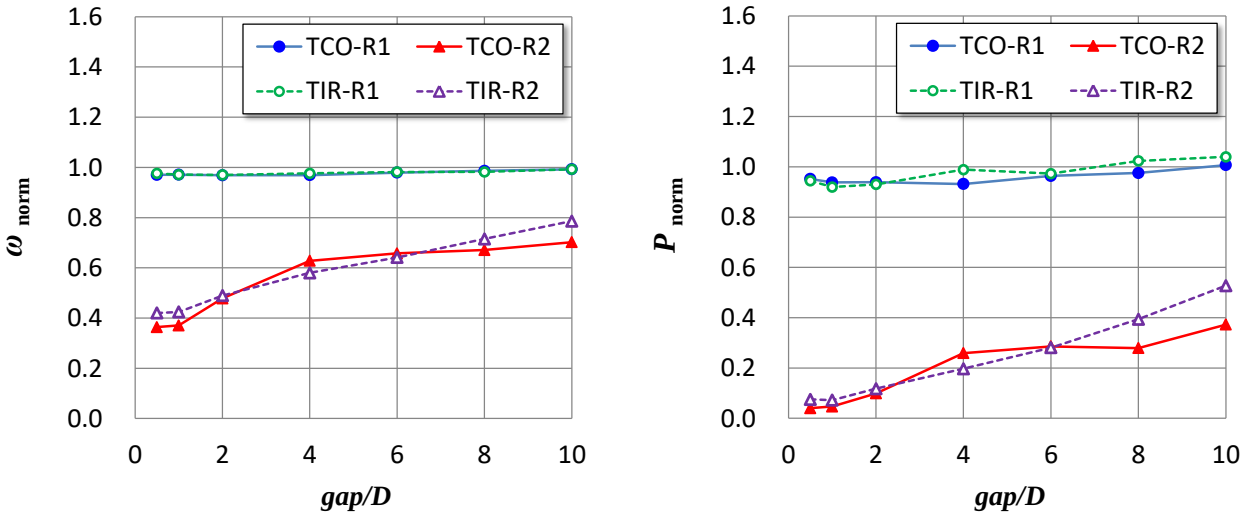

(a) ω_{norm} vs gap/D (b) P_{norm} vs gap/D

Figure 12. Gap dependence of (a) normalized angular velocity and (b) normalized power of each rotor in tandem layouts.

3.3. Gap and Wind Direction Dependence of 16-direction Layouts

The 16-wind-direction dependence of the normalized angular velocity in the CO and IR configurations with gap lengths of gap/D = 0.5, 1, and 2 are shown in Figures 13(a)-(f). In each figure, the blue circles indicate the angular velocity ω_1 of R1, and the red triangle symbols the angular velocity ω_2 of R2. The white squares represent the mean values of both rotors. The green circle corresponds to the case of an isolated single rotor. In all the figures, the angular velocity of the downwind rotor R2 in the tandem layout of the wind direction of θ = 90° decreases significantly; similarly, that of the downwind rotor R1 in the tandem layout of θ = 270° decreased. In the case of gap/D = 0.5 (see Figures 13(a) and (b)), the extent of decrease in the angular velocity of the downwind-side rotor was the second largest in wind directions of θ = 112.5° and 292.5° in the CO configuration; meanwhile, it was the second largest for the tandem case in wind directions of θ = 112.5° and 247.5° in the IR configuration. This difference is attributed to the symmetry of the configurations, and in all the figures illustrating the distributions of the mean normalized angular velocity of the two rotors, the CO configuration exhibited the origin symmetry, whereas the IR configuration exhibited line symmetry with respect to the line connecting the wind directions of θ = 0° and 180° . In the case of gap/D = 1 shown in Figures 13(c) and (d), the bias of distribution, i.e., the decrease in the angular velocity at θ = 112.5° and 292.5° observed in the case of gap/D = 0.5, reduced in the CO configuration; however, the bias was evident in the IR configuration. This is due to the significant wake deflection of the upwind rotor in the IR configurations, as shown by the comparison between Figures 11(b) and (d). However, approaching gap/D = 2, the angular velocity distributions of both the CO and IR configurations exhibited similar shapes with less bias. This finding can be explained as follows: when the gap length became more than twice the rotor diameter, the downwind-side rotor located in the direction of $\Delta\theta$ = ±22.5° to the main flow was less affected by the wake of the upwind rotor in any configuration. Focusing on the neighborhoods of θ = 0° and 180° as well as including the parallel layouts, in the CO configuration, the angular velocities in both neighborhoods were similar and larger than that of an isolated single rotor. Meanwhile, in the IR configuration, the angular velocities of R1 and R2 in the neighborhood of θ = 0° were higher than that of an isolated single rotor. However, in the neighborhood of θ = 180°, the angular velocities of both rotors were similar to that of an isolated single rotor, or the angular velocity of one rotor was higher than and that of the other rotor was lower than the angular velocity of an isolated single rotor.

 doi:10.20944/preprints202103.0527.v1

The 16-wind-direction dependence of the normalized power shown in Figure 14 emphasizes the characteristics observed in Figure 13 for the distributions in the normalized angular velocity. Although the bias in the power distributions in the case of gap/D = 2 (Figures 14(e) and (f)) decreased compared with the case of a short gap, the distributions between the CO and IR configurations differed. In the CO configuration, the power of R2 was larger than that of R1 in wind directions of θ = 0°–67.5° (inversely, the power of R1 was larger than that of R2 in wind directions of θ = 180°–247.5°). Meanwhile, in the IR configuration, the power of R2 was larger than that of R1 in wind directions of θ = 135°–157.5° (inversely, the power of R1 was larger than that of R2 in wind directions of θ = 202.5°–225°).

A comparison of the 16-direction dependence of the mean normalized power of the two rotors is shown in Figure 15. Focusing on the neighborhoods of θ = 0° and 180° as well as including the parallel layouts, in the CO configuration, the mean normalized powers in both neighborhoods were similar and exceeded that of an isolated single rotor, regardless of the gap space. The maximum rotor power averaged for three gap lengths was approximately 16% higher than the power of an isolated single rotor. In the IR configuration, the mean normalized powers in the neighborhood of θ = 0° were much higher than the power of an isolated single rotor (the maximum increase averaged for three gap lengths was approximately 22%). However, in the neighborhood of θ = 180°, the mean normalized power barely exceeded the power of an isolated single rotor (the maximum increase averaged for three gap lengths was approximately 6%). The power distributions in the CO and IR configurations for gap/D = 2 exhibited similar shapes and slight bias, except for the neighborhoods of θ = 0° and 180°.

Preprints (www.preprints.org) | NOT PEER-REVIEWED | Posted: 22 March 2021 doi:10.20944/preprints202103.0527.v1

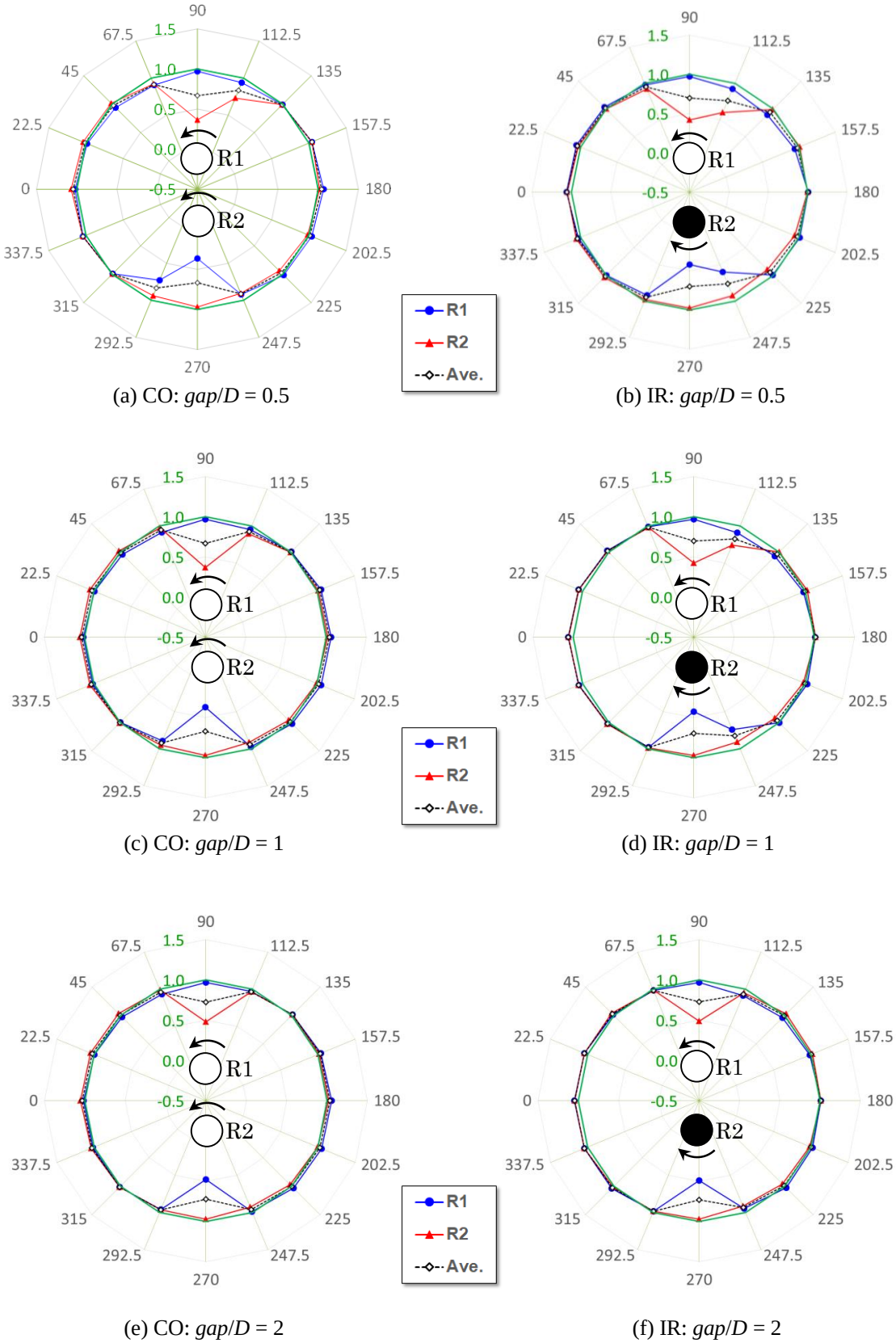

(a) CO: *gap*/*D* = 0.5

(b) IR: *gap*/*D* = 0.5

(c) CO: *gap*/*D* = 1

(d) IR: *gap*/*D* = 1

(e) CO: *gap*/*D* = 2

(f) IR: *gap*/*D* = 2

Figure 13. 16-wind-direction dependence of normalized angular velocity: (a) CO configuration, *gap*/*D* = 0.5; (b) IR configuration, *gap*/*D* = 0.5; (c) CO configuration, *gap*/*D* = 1; (d) IR configuration, *gap*/*D* = 1; (e) CO configuration, *gap*/*D* = 2; (f) IR configuration, *gap*/*D* = 2.

Preprints (www.preprints.org) | NOT PEER-REVIEWED | Posted: 22 March 2021 doi:10.20944/preprints202103.0527.v1

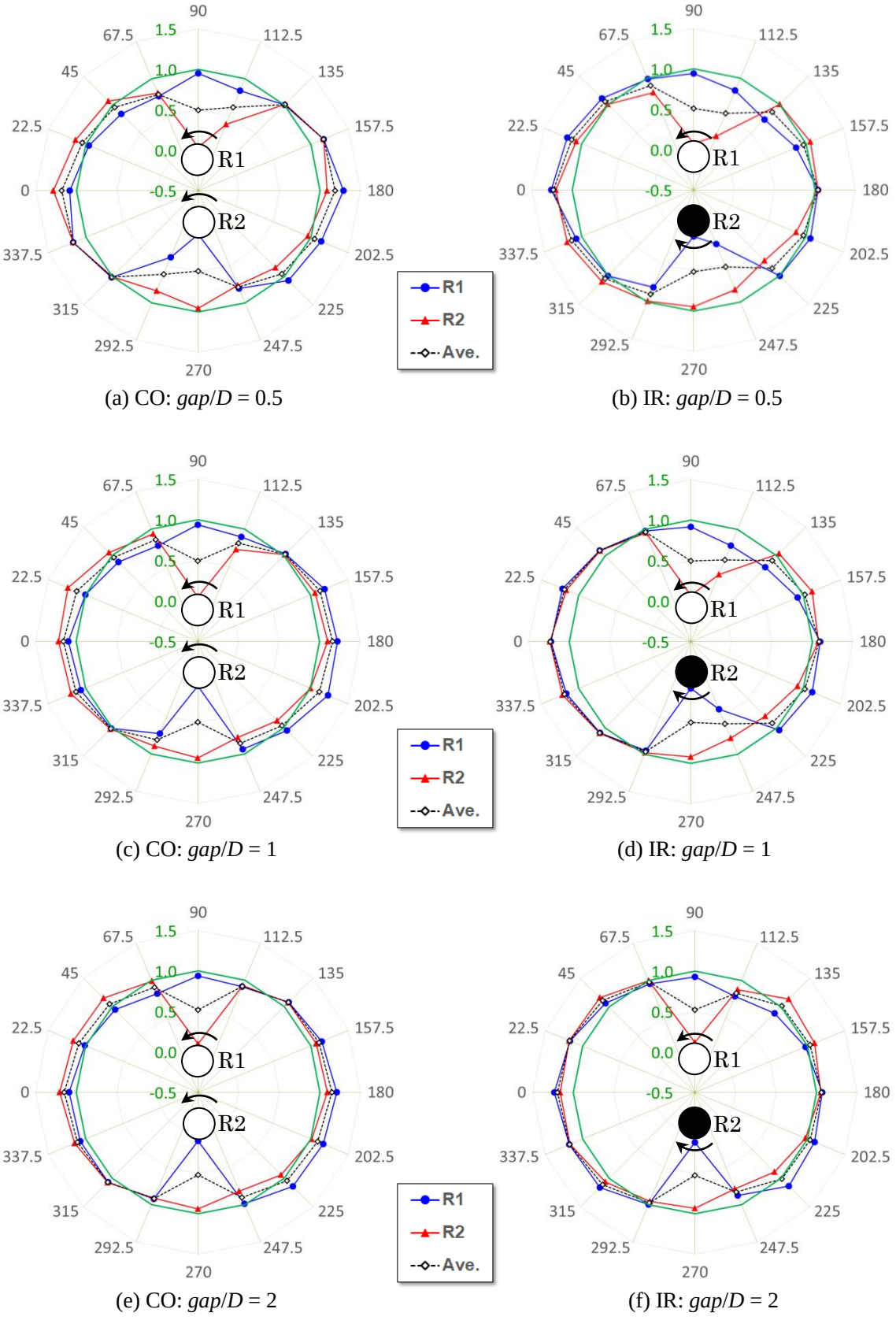

(a) CO: *gap*/*D* = 0.5

(b) IR: *gap*/*D* = 0.5

(c) CO: *gap*/*D* = 1

(d) IR: *gap*/*D* = 1

(e) CO: *gap*/*D* = 2

(f) IR: *gap*/*D* = 2

Figure 14. 16-wind-direction dependence of normalized power: (a) CO configuration, *gap*/*D* = 0.5; (b) IR configuration, *gap*/*D* = 0.5; (c) CO configuration, *gap*/*D* = 1; (d) IR configuration, *gap*/*D* = 1; (e) CO configuration, *gap*/*D* = 2; (f) IR configuration, *gap*/*D* = 2.

Preprints (www.preprints.org) | NOT PEER-REVIEWED | Posted: 22 March 2021 doi:10.20944/preprints202103.0527.v1

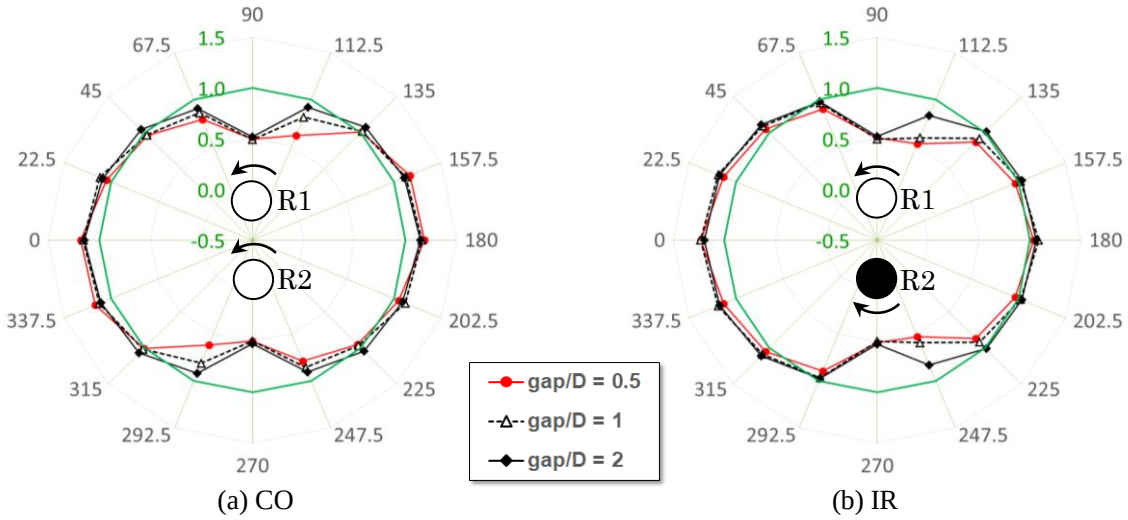

(a) CO (b) IR

Figure 15. 16-direction dependence of average of normalized power: (a) CO configuration; (b) IR configuration.

The simple average of the normalized powers of the 16 wind directions is tabulated for each gap length and configuration in Table 2. These values correspond to the ratios of the expected output power per rotor to that of an isolated single rotor under the assumption of an isotropic 16-directional wind speed. The simply averaged power in the CO configuration was higher than that in the IR configuration, regardless of the gap length. The difference between the two configurations decreased as the gap space increased.

Table 2. Simple average of normalized powers under assumption of isotropic 16-directional wind speed.

Configuration	*gap/D* = 0.5	*gap/D* = 1	*gap/D* = 2
CO	0.909	0.945	0.976
IR	0.886	0.929	0.975

3.4. Phase Synchronization of Rotor Pair

Figure 16 shows the DFBI-CFD analysis results of angular velocities of two rotors in the CD layout with a gap length of gap/D = 0.2, where the initial angular velocities were set at different values (R1: ω_1 = 366 rpm; R2: ω_2 = 385 rpm). The broken line expresses the difference between the angular velocities of the two rotors, i.e., $\Delta\omega = \omega_1 - \omega_2$. After 2 s from the start of the calculation, the two angular velocities ω_1 and ω_2 showed similar values but begin to alternate in terms of the magnitude correlation. The angular velocity difference $\Delta\omega$ varied by changing the sign at an almost constant period. This phenomenon corresponds to the phase synchronization observed experimentally by Vergaerde et al. [13] and Jodai et al. [16, 17]; to the best of our knowledge, the results shown in Figure 16 are the first reproduction of the phase synchronization of two VAWT rotors via CFD analysis.

Preprints (www.preprints.org) | NOT PEER-REVIEWED | Posted: 22 March 2021 doi:10.20944/preprints202103.0527.v1

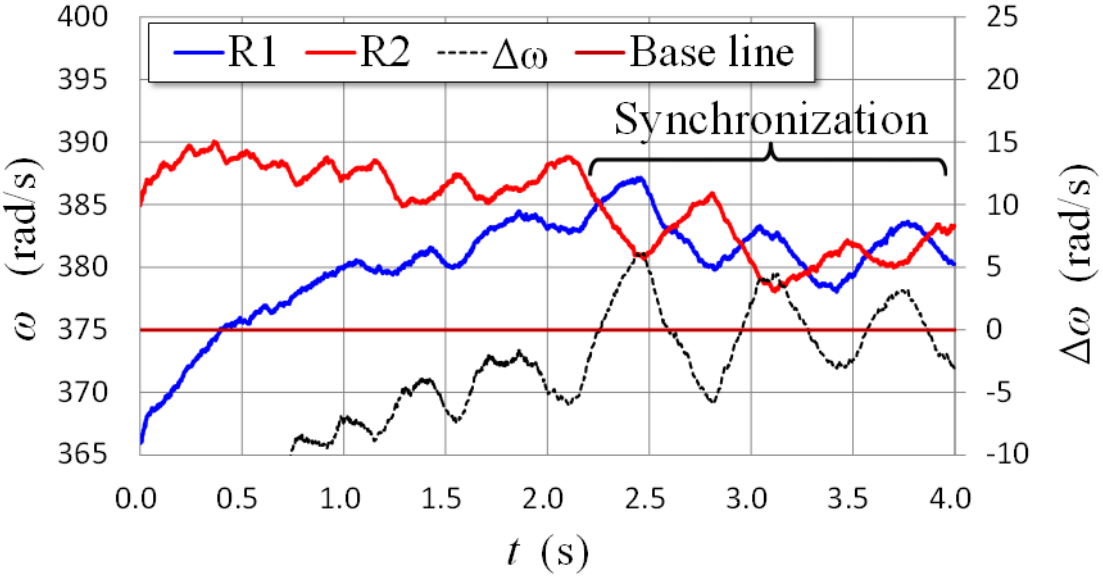

Figure 16. State of phase synchronization in angular velocities of two rotors in CD layout with *gap*/*D* = 0.2.

Although Figure 17 corresponds to the same CD layout with *gap*/*D* = 0.2, as shown in Figure 16, the values calculated using the identical initial value (366 rpm) for both rotors are shown in Figure 17, the data of which are equivalent to those shown in Figures 8(b) and 9(b). The green broken line shows the difference in the angular velocities of the two rotors, and the orange broken line shows the difference in the torques $\Delta Q = Q_1 - Q_2$. The torque difference shown in Figure 17 was obtained using the moving average of the original torque data with a time width of 0.1 s because the torque fluctuation was severe. To be consistent with the averaging time width of the torque difference, the angular velocity difference is illustrated using the moving average processed with the same time width of 0.1 s, as in Figure 17. Both $\Delta\omega$ and ΔQ varied by sign change at a constant period of approximately 0.7 s, and the phase of ΔQ resulted in $\Delta\omega$ varying by $\pi/2$. A similar phenomenon was observed in the CU layout with *gap*/*D* = 0.2 and 0.3. The time period of the variations in $\Delta\omega$ and ΔQ increased as the gap space widened. The period was approximately 1 s in the CU layout with *gap*/*D* = 0.3.

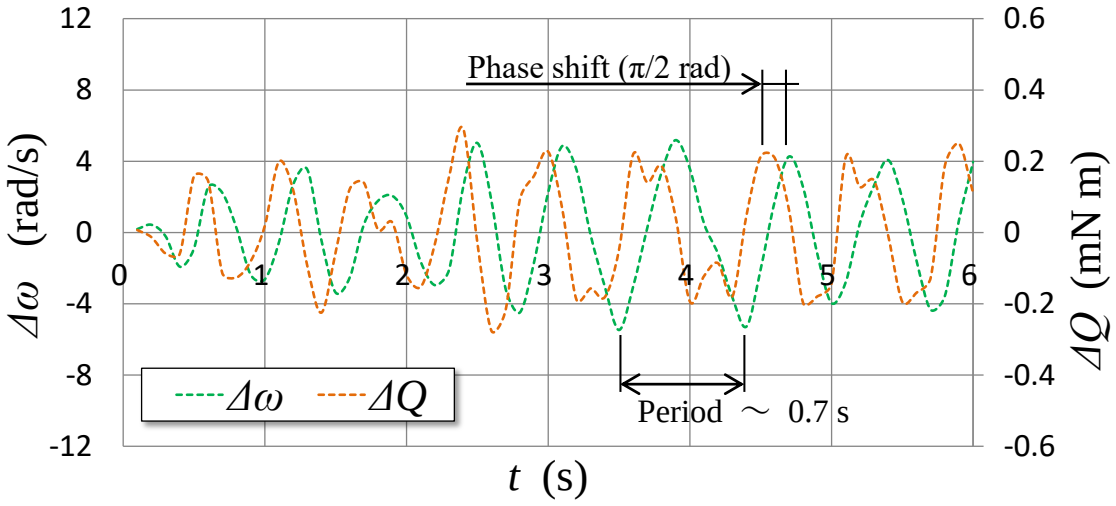

Figure 17. Phase shift between difference in angular velocities and that in torques, of two rotors in phase synchronization for CD layout with *gap*/*D* = 0.2 (data do not correspond to Figure 16 but Figures 8(b) and 9(b)).

Preprints (www.preprints.org) | NOT PEER-REVIEWED | Posted: 22 March 2021 doi:10.20944/preprints202103.0527.v1

The angular velocities (ω_1 and ω_2) of the two rotors and the difference $\Delta\omega$ are illustrated for the CD layout with gap/D = 0.3, as shown in Figure 18. The data shown in Figure 18 indicate the most significant fluctuation among the data managed in this study. The RMS of ω_1 in the final 1 s (14–15 s), in which the data for Figure 18 were averaged to obtain the converged results, was 4.42 rad/s, and the gradient of the linear approximation was -6.34 rad/s^2. In this example, the two angular velocities indicated almost similar values, but the angular velocity difference $\Delta\omega$ did not exhibit regular periodicity. In fact, by observing the movements of the blades simulated from the DFBI-CFD analysis, a small in-phase time zone was observed. In other words, phase synchronization was not observed in the CD layout with gap/D = 0.3. As mentioned above, however, phase synchronization was observed in the case of gap/D = 0.3 of the CU layout. Vergaerde et al. reported the instability of phase synchronization in a CD layout compared with that in a CU layout in their experiments [13]. The difference in the torque behavior between the CD and CU layouts in the region of short gap length shown in Figures 9(b) and (c) might be ascribed to the instability of the CD layout.

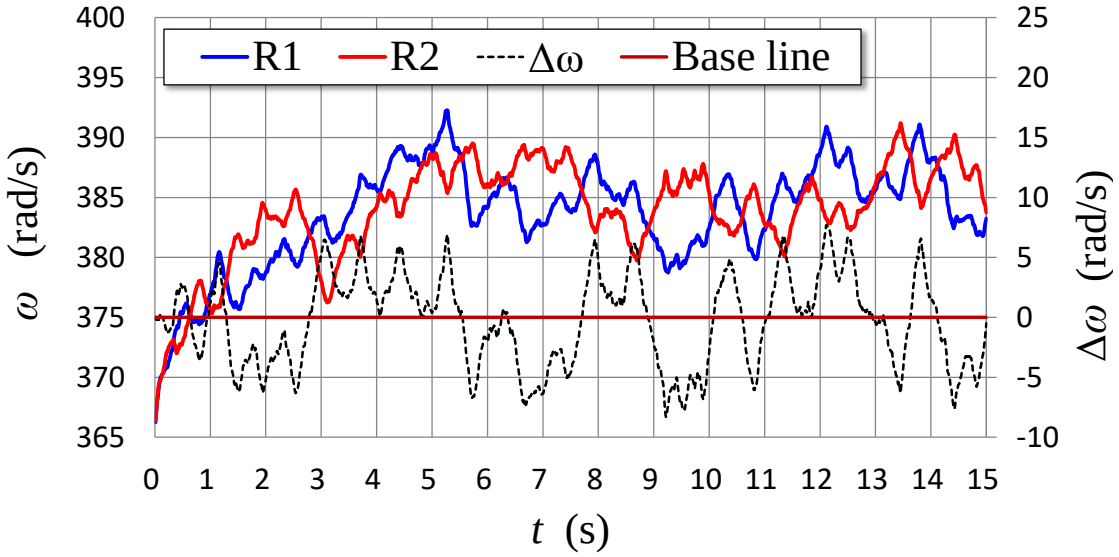

Figure 18. Out-of-phase state for angular velocities of two rotors in CD layout with gap/D = 0.3.

Next, the mechanism of phase synchronization generation was considered. Figure 19 shows the color contour of the flow velocity (x-direction component) around the rotors in a state of phase synchronization in the CD layout with gap/D = 0.2, which corresponds to the data in Figure 16. As illustrated in Figure 19, the blades of the two rotors rotated in phase. The fluid accelerated in the area between the blades that approached the minimal gap between the two rotors. From this observation and based on Bernoulli's law, the pressure was reduced in the area sandwiched by the approaching blades. Consequently, the approaching blades with some phase difference mutually generated attractive forces, as illustrated in Figure 20; a delayed blade was accelerated and a leading blade was decelerated; this state might alternate at a constant period. Consequently, variations occurred in the angular velocity and torque, as shown in Figures 16 and 17.

Preprints (www.preprints.org) | NOT PEER-REVIEWED | Posted: 22 March 2021 doi:10.20944/preprints202103.0527.v1

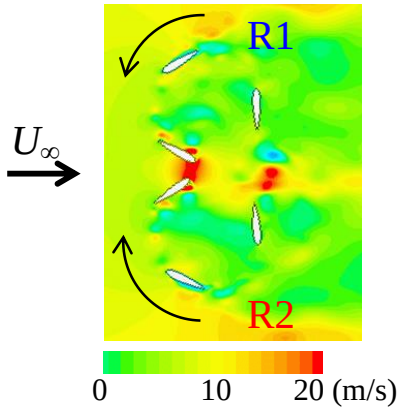

Figure 19. Color contour of flow velocity (x-direction component) around rotors in CD layout with gap/D = 0.2, where increase in flow speed by phase synchronization of two rotors is demonstrated.

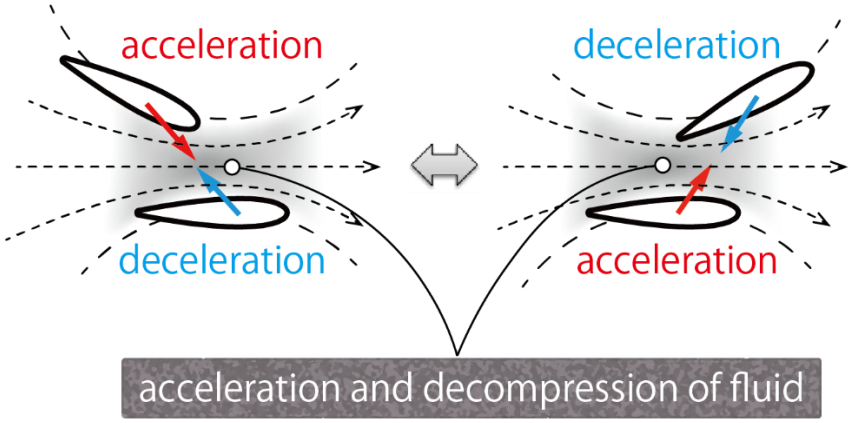

Figure 20. Expected principle of phase synchronization in closely spaced wind turbines.

4. Conclusions

In this study, CFD simulations were performed for a 2D closely spaced VAWT rotor pair using the DFBI method. The CD layout yielded a higher average power of the two rotors than the CU layout owing to the effects of induced velocity. The average power of the two rotors in the CD layout with gap/D = 0.5–1 was 23% higher than the power of an isolated single rotor. In the case involving a long gap in the tandem layouts, the downwind rotor in the TIR layout tended to generate more power than that in the TCO layout. This is attributed to the wake deflection caused by the induced velocity of the downwind rotor. Under the assumption of a virtual isotropic wind speed distribution, the mean power generated in the CO configuration was higher than that in the IR configuration. When the gap space reached twice the rotor diameter, the 16-wind-direction distribution in terms of the averaged power of the two rotors in the CO and IR configurations became similar. The present study demonstrated the phase synchronization of two VAWT rotors via CFD analysis for the first time. In the synchronized state, the phase of torque difference between the two rotors investigated advanced that of the angular velocity difference by $\pi/2$. The mechanism of phase synchronization, as explained based on Bernoulli's law, was attributed to the acceleration and decompression of fluid between mutually approaching blades.

Author Contributions: Conceptualization, Y.H. and Y.J.; methodology, Y.H.; software, Y.H.; validation, Y.J. and M.F.; formal analysis, Y.H. and T.O.; investigation, Y.J.; resources, Y.H.; data curation, Y.H. and T.O.; writing—original draft preparation, Y.H.; writing—review and editing, Y.J. and M.F.; visualization, Y.H. and T.O..; supervision, Y.H.; project administration, Y.H.; funding acquisition, Y.H. and Y.J. All authors have read and agreed to the published version of the manuscript.

Funding: This research was supported by JSPS KAKENHI Grant Number JP 18K05013 and the International Platform for Dryland Research and Education (IPDRE), Tottori University.

Data Availability Statement: The data that support the findings of this study are available from the corresponding author, Y.H., upon reasonable request.

Acknowledgments: The authors would like to thank Shu Yamamoto for conducting the CFD analysis in the early stages of the study. The authors would like to thank Editage (www.editage.com) for English language editing.

Conflicts of Interest: The authors declare no conflict of interest.

References

1. Göçmen, T.; Laan, P. v. d.; Réthoré, P.-E.; Diaz, A. P.; Larsen, G. C.; Ott, S. Wind turbine wake models developed at the technical university of Denmark: A review. *Renewable Sustainable Energy Rev.* **2016,** 60, pp. 752-769. [10.1016/j.rser.2016.01.113]
2. Shao, Z.; Wu, Y.; Li, L.; Han, S.; Liu, Y. Multiple Wind Turbine Wakes Modeling Considering the Faster Wake Recovery in Overlapped Wakes. *Energies* **2019,** 12, (4), p. 680. [10.3390/en12040680]
3. Rajagopalan, R. G.; Rickerl, T. L.; Klimas, P. C. Aerodynamic interference of vertical axis wind turbines. *J. Propul. Power* **1990,** 6, (5), pp. 645-653. [10.2514/3.23266]
4. Whittlesey, R. W.; Liska, S.; Dabiri, J. O. Fish schooling as a basis for vertical axis wind turbine farm design. *Bioinspiration Biomimetics* **2010,** 5, (3), p. 035005. [10.1088/1748-3182/5/3/035005]
5. Dabiri, J. O. Potential order-of-magnitude enhancement of wind farm power density via counter-rotating vertical-axis wind turbine arrays. *J. Renewable Sustainable Energy* **2011,** 3, (4), p. 043104. [10.1063/1.3608170]
6. Kinzel, M.; Mulligan, Q.; Dabiri, J. O. Energy exchange in an array of vertical-axis wind turbines. *J. Turbul.* **2012,** 13, p. N38. [10.1080/14685248.2012.712698]
7. Zanforlin, S.; Nishino, T. Fluid dynamic mechanisms of enhanced power generation by closely spaced vertical axis wind turbines. *Renewable Energy* **2016,** 99, pp. 1213-1226. [10.1016/j.renene.2016.08.015]
8. Chen, W.-H.; Chen, C.-Y.; Huang, C.-Y.; Hwang, C.-J. Power output analysis and optimization of two straight-bladed vertical-axis wind turbines. *Appl. Energy* **2017,** 185, pp. 223-232. [10.1016/j.apenergy.2016.10.076]
9. De Tavernier, D.; Ferreira, C.; Li, A.; Paulsen, U. S.; Madsen, H. A. Towards the understanding of vertical-axis wind turbines in double-rotor configuration. *J. Phys. Conf. Ser.* **2018,** 1037, p. 022015. [10.1088/1742-6596/1037/2/022015]
10. Ma, Y.; Hu, C.; Li, Y.; Li, L.; Deng, R.; Jiang, D. Hydrodynamic Performance Analysis of the Vertical Axis Twin-Rotor Tidal Current Turbine. *Water* **2018,** 10, (11), p. 1694. [10.3390/w10111694]
11. Bearman, P. W.; Wadcock, A. J. The interaction between a pair of circular cylinders normal to a stream. *J. Fluid Mech.* **1973,** 61, (3), pp. 499-511. [10.1017/S0022112073000832]
12. Yoon, H. S.; Chun, H. H.; Kim, J. H.; Ryong Park, I. L. Flow characteristics of two rotating side-by-side circular cylinder. *Comput. Fluids* **2009,** 38, (2), pp. 466-474. [10.1016/j.compfluid.2008.09.002]
13. Vergaerde, A.; De Troyer, T.; Kluczewska-Bordier, J.; Parneix, N.; Silvert, F.; Runacres, M. C. Wind tunnel experiments of a pair of interacting vertical-axis wind turbines. *J. Phys. Conf. Ser.* **2018,** 1037, p. 072049. [10.1088/1742-6596/1037/7/072049]
14. Hara, Y.; Jodai, Y. Study on Close Arrangement of Small Vertical Axis Wind Turbines. *Turbomach.* **2021,** 49, (1), pp. 13-21.

15. Hara, Y.; Tagawa, K.; Saito, S.; Shioya, K.; Ono, T.; Makino, K.; Toba, K.; Hirobayashi, T.; Tanaka, Y.; Takashima, K.; Sasaki, S.; Nojima, K.; Yoshida, S. Development of a Butterfly Wind Turbine with Mechanical Over-Speed Control System. *Designs* **2018,** 2, (2), p. 17. [10.3390/designs2020017]
16. Jodai, Y.; Hara, Y.; Sogo, Y.; Marusasa, K.; Okinaga, T. Wind tunnel experiments on interaction between two closely spaced vertical axis wind turbines, Proc. The 23rd Chu-Shikoku-Kyushu Branch Meeting, JSFM, 2019/6/1-2, 11.1-2.
17. Jodai, Y.; Hara, Y. Wind tunnel experiments on interaction between two closely spaced vertical axis wind turbines in parallel arrangements. *Fluid Dyn. Res.* **2021,** (under review).
18. Zhang, Y.; Kim, B. A Fully Coupled Computational Fluid Dynamics Method for Analysis of Semi-Submersible Floating Offshore Wind Turbines Under Wind-Wave Excitation Conditions Based on OC5 Data. *Appl. Sci.* **2018,** 8, (11), p. 2314. [10.3390/app8112314]
19. Yamamoto, S.; Hara, Y.; Jodai, Y. Numerical analysis on dynamic interaction between two closely spaced vertical axis wind turbines, Proc. The 57th Chugoku-Shikoku Branch Meeting, JSME, 2019/3/7, K604.
20. Okinaga, T.; Hara, Y.; Jodai, Y. Numerical analysis on the averaged power of a vertical axis wind turbine pair against 16-direction wind distributions, Proc. 2020 Annual General Meeting, JSME, 2020/9/16, J05309.
21. Hara, Y.; Jodai, Y.; Yamamoto, S.; Okinaga, T. Numerical Simulation on Tandem Layout of Two Vertical Axis Wind Turbines, Proc. 2019 Annual General Meeting, JSME, 2019/9/10, J05325.
22. Hara, Y.; Jodai, Y.; Okinaga, T.; Sogo, Y.; Kitoro, T.; Marusasa, K. A synchronization phenomenon of two closely spaced vertical axis wind turbines, Proc. The 25th Chu-Shikoku-Kyushu Branch Meeting, JSFM, 2020/5/31, 3.1-2.
23. Menter, F. R. Two-equation eddy-viscosity turbulence models for engineering applications. *AIAA J.* **1994,** 32, (8), pp. 1598-1605. [10.2514/3.12149]
24. Sumner, D. Two circular cylinders in cross-flow: A review. *J. Fluids Struct.* **2010,** 26, (6), pp. 849-899. [10.1016/j.jfluidstructs.2010.07.001]
25. Miyashita, A.; Hara, Y.; Yoshida, S.; Sumi, T.; Akimoto, H. The effects of arms on the averaged wake of a straight-bladed vertical axis wind turbine with the inclined rotational axis, Proc. The 50th Student Member Presentation of Graduation Theses, Chugoku-Shikoku Branch Meeting, JSME, 2020/3/5, S04b2.